

Inherent Stability Modes of Low-Aspect-Ratio Wings

Matt Shields* and Kamran Mohseni†
University of Florida, Gainesville, Florida 32611-6250

DOI: 10.2514/1.C032636

The development of micro aerial vehicles has been hindered by a poor understanding of the flight dynamics associated with the unique aerodynamic regime. This study experimentally estimates the aerodynamic damping derivatives of flat-plate wings with aspect ratios less than 3 at a Reynolds number of 7.5×10^4 ; when combined with previously published results detailing the lateral and longitudinal static loads, a dynamic model is developed for low-aspect-ratio wings. The initial-condition response of the linear equations of motion shows that the loading created by roll stall results in purely aerodynamic lateral modes which, unlike conventional aircraft, are not attributed to geometric features, such as the vertical tail; this response was favorably compared with the integration of the full nonlinear equations. The mode is manifested by divergent, high-amplitude perturbations in sideslip, bank angle, and roll rate; furthermore, it is seen to be affected by angle of attack variations, which significantly alter the instantaneous value of the roll stability derivative L_{β} . If the input frequency of the angle of attack oscillations is close to the natural frequency of the pure lateral mode, the bank angle is seen to drift away from its equilibrium value due to an attenuated restoring roll moment. This represents a previously unconsidered stability mode, referred to as roll-resonance, which couples the lateral and longitudinal stability axes for small perturbations from equilibrium flight conditions.

Nomenclature

b	=	wingspan, cm
C	=	damping term in differential equation, N/(rad/s)
c	=	chord, cm
f	=	motion frequency, Hz
f_c	=	low-pass-filter cutoff frequency, Hz
f_s	=	data sampling frequency, Hz
I	=	moment of inertia, $\text{kg} \cdot \text{m}^2$
$I_x, I_y, I_z, I_{xz}, I_{yz}$	=	moments of inertia about body axes, $\text{kg} \cdot \text{m}^2$
K	=	spring term in differential equation, N/rad
k	=	reduced frequency, $k = fb/2U_0$
L, M, N	=	body moment components, $\text{N} \cdot \text{m}$
p, q, r	=	body components of rotational velocity, deg/s
t_{lag}	=	time delay between model motion and aerodynamic load, s
U_0	=	freestream velocity, m/s
u, v, w	=	body components of translational velocity, m/s
v	=	eigenvector
X, Y, Z	=	body force components, N
x_{lat}	=	lateral state vector
x, y, z	=	body centered axes
α	=	angle of attack, deg
β	=	sideslip angle, deg
γ	=	sample displacement variable
γ_w	=	test-function displacement, deg
$\gamma_{w,\text{lag}}$	=	test-function delayed displacement, deg
ζ	=	damping ratio

θ	=	pitch angle, deg
λ	=	eigenvalue
Φ, Θ, Ψ	=	Euler angles, deg
ϕ	=	bank angle, deg
ω	=	angular velocity, rad/s
$\omega_{n,\text{lat}}$	=	natural angular velocity of lateral mode, rad/s
ω_α	=	angular velocity of prescribed $\alpha(t)$, rad/s

I. Introduction

SIGNIFICANT progress has been recently made in the development of novel, bioinspired micro aerial vehicles (MAVs) ranging from flexible/morphing wing aircraft to nano- and pico-scale flapping-wing flyers [1–6]. The design of these vehicles has been predominantly based upon iterative flight-testing methods due to the lack of availability of aerodynamic design tools for this complex regime, in which interactions between separated flow and tip-vortex effects strongly influence the aerodynamic loading under static and dynamic conditions [7–15]. While the increasing availability of wind-tunnel results for low-aspect-ratio (LAR) low-Reynolds-number wings has provided some baseline data for MAV designers, this has typically been restricted to longitudinal loading (lift, drag, pitching moment) of assorted planforms [16–19]. Recently published results by the authors have demonstrated that the lateral loading of LAR wings experiences a significant roll moment due to roll stall, an asymmetric loading condition created by asymmetric tip vortices in sideslip; this results in large magnitudes of the roll stability derivative L_{β} , and has significant implications for vehicle control and gust rejection [20–23].

The lateral response characteristics of aircraft have historically been attributed to the influence of a number of geometric factors, including the side forces and moments generated by the vertical tail, the antisymmetric loading of wings with sweep or dihedral, and the displacement of streamlines by the fuselage; the impact of these parameters was recognized in the earliest days of aviation, and has become standard knowledge available in aircraft dynamics textbooks [24–27]. An example of oscillatory lateral motion is the Dutch-roll response, which is a periodic response of sideslip, roll, and yaw, and is typically stable for correctly sized vertical-tail surfaces [28]. A rotation of the aircraft about its center of gravity induces static and dynamic loading dependencies due to these geometric asymmetries about the plane of the wing; these typically required empirical wind-tunnel data to provide reliable estimates of the associated magnitudes [24]. The challenges involved in designing a laterally stable MAV suggest that the aerodynamic regime itself is a fundamental cause of

Presented as Paper 2013-4939 at the AIAA Guidance, Navigation and Controls Conference, Boston, MA, 19–22 August 2013; received 17 September 2013; revision received 29 January 2014; accepted for publication 8 February 2014; published online 10 September 2014. Copyright © 2014 by the American Institute of Aeronautics and Astronautics, Inc. All rights reserved. Copies of this paper may be made for personal or internal use, on condition that the copier pay the \$10.00 per-copy fee to the Copyright Clearance Center, Inc., 222 Rosewood Drive, Danvers, MA 01923; include the code 1542-3868/14 and \$10.00 in correspondence with the CCC.

*Graduate Research Assistant, Department of Mechanical and Aerospace Engineering, Student Member AIAA.

†William P. Bushnell Endowed Chair in Mechanical and Aerospace Engineering Department and Electrical and Computer Engineering Department, Institute for Networked Autonomous Systems, Associate Fellow AIAA.

the instabilities; specifically, the presence of roll stall on LAR wings is associated with the increased impact of tip vortices when the wingspan is sufficiently small, and has been discussed as an underlying factor in gust sensitivity and loss of control during banked turns [20]. To address this, the models tested in this experiment are designed to remove the aforementioned geometric features by testing simple flat plates, which make it possible to isolate the impact of the flow behavior on the static and dynamic stability characteristics of the wing.

A full investigation into the inherent dynamics of LAR wings requires estimates of the aerodynamic damping derivatives; this type of survey using canonical flat-plate wings has not been conducted at low Reynolds numbers due to the associated experimental challenges. The authors have updated their experimental setup at the University of Florida to enable these measurements in all relevant degrees of freedom (roll, pitch, yaw, plunge) using a forced-oscillation technique [29]. The availability of all potential static and dynamic load dependencies for the first time in a Reynolds-number regime applicable to MAVs permits the development of a dynamic model for LAR wings; this paper describes how the nature of the loads created by roll stall provides unique, coupled stability modes, which are attributed to the flow effects and inertial properties of the wings. Similar types of investigations have been previously conducted to characterize the nonlinear aerodynamic effects and stability-analysis methods, such as wing rock, inertial coupling, unsteady aerodynamics, buffeting, and the application of catastrophe theory; the reader is referred to the list of provided review publications, which describes these in great detail [27,30–37]. It should be noted, however, that these aforementioned modes are typically present at the maneuverability limits of high-performance aircraft, and that the bulk of the existing literature refers to higher-Mach-number regimes. The results presented in this paper for rectangular LAR wings are applicable to the low-Reynolds-number, fully incompressible flight regime of MAVs (Mach number ~ 0.03), and are also shown to occur at cruising flight conditions. As such, they have critical implications for future MAV designers, as it is necessary to consider the inherent dynamics of the wing before incorporating the additional effects of geometric features in the quest to design a passively stable vehicle.

The outline of this paper is as follows: the experimental setup and methodology used to collect the damping derivatives are summarized in Sec. II. The measured values of these derivatives are plotted and described in Sec. III. The simulation results for the nonlinear equations of motion are depicted in Sec. IV and are compared with linear models, which are used to describe the parameters of the stability modes. Finally, the relevant conclusions of the study, with respect to the impact of these results on future MAV design, are discussed.

II. Methodology

A. Experimental Setup: Wind Tunnel and Force Balance

All experimental results collected in this investigation were obtained using the Prototunnel located at the University of Florida campus, which has previously been described in detail by the authors [19]. Results are presented for a flat-plate wing (0% camber) with an aspect ratio of unity ($b = c = 10.2$ cm), a 5:1 elliptically rounded leading edge, and a thickness-to-chord ratio of 1.6%; aspect ratios of $\mathcal{R} = 1.5$ and 2 were also tested, although, as the dynamics were similar to those of the $\mathcal{R} = 1$ case, the results are not discussed in this paper for brevity. This result is not entirely surprising, as previous results by the authors indicated that the behavior of roll stall, which will be shown to be the driving mechanism for the lateral-stability modes of LAR wings, is similar for aspect ratios below 3 [20]. Testing of aspect ratios above 2 is not currently feasible due to the geometric constraints of the Prototunnel and the inertial limitations of the model positioning system (MPS) motors. Figure 1 shows a schematic depicting the model placement relative to the force balance and MPS in the tunnel, in addition to relevant coordinate axes and the definition of sideslip angle (which is defined as negative when there is a flow

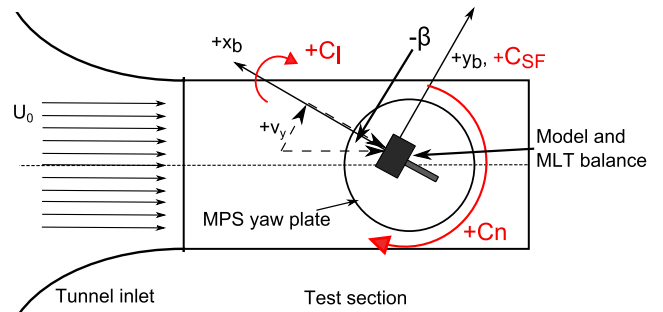


Fig. 1 Top view of Prototunnel test section showing body-fixed coordinate system.

component moving in the $+y_b$ axis, as this corresponds to the wing translating in a positive flight direction [27]).

B. Forced-Oscillation Technique

While a number of experimental methods exist for the estimation of aerodynamic damping derivatives, accurate results have been notoriously difficult to obtain [38]. Techniques such as free oscillations, forced oscillations, curved-flow tunnels, and free-flight testing have been applied to a wide variety of aircraft configurations to obtain first-order estimates of damping parameters [39–45]. The MPS was designed and built by the group to conduct forced-oscillation testing, which permits the testing of different degrees of freedom and angular/translational rates; this is desirable for LAR wings, as no systematic investigations of the damping parameters have previously been conducted for this unique low-Reynolds-number regime. The potential high incidence angles and susceptibility to large gust perturbations common to the MAV regime require the characterization of these derivatives for a wide variety of conditions.

Aerodynamic damping is an out-of-phase loading, which opposes the translational and angular velocities of a wing (or aircraft) in a manner physically identical to a dashpot damper in a dynamic systems analysis [38,46]. As such, forced-oscillation testing is designed to intentionally generate a motion profile representative of a harmonic oscillator. As the displacement of the wing can be modeled by a second-order linear differential equation with a known solution, the damping constant can be extracted.

The motion of a forced, periodic oscillator with constant damping and a linear relationship between the angular displacement of the model γ and the forcing term $F_0 \cos(\omega t)$ is represented by the differential equation:

$$\ddot{\gamma} + C\dot{\gamma} + K\gamma = F_0 \cos(\omega t) \quad (1)$$

in which C is the (constant) damping term, K is the restorative spring term, and ω is the angular velocity of the motion (with all terms normalized by moment of inertia) [46]. The solution of this equation can be expressed in the form $\gamma(t) = \gamma_0 \cos(\omega t + \delta)$, in which δ represents the phase lag between the forcing term and the motion of the body. The position, velocity, and acceleration of γ can be expanded using trigonometric identities, and grouped into $\sin(\omega t)$ and $\cos(\omega t)$ terms:

$$-\gamma_0 \omega^2 \cos \delta + C\gamma_0 \omega \sin \delta + K\gamma_0 \cos \delta = F_0 \quad (2)$$

$$-\gamma_0 \omega^2 \sin \delta - C\gamma_0 \omega \cos \delta + K\gamma_0 \sin \delta = 0 \quad (3)$$

Equations (2) and (3) can then be simultaneously solved for the damping constant C and a spring term $K - \omega^2$:

$$C = \frac{F_0 \sin \delta}{\omega \gamma_0} \quad (4)$$

$$K - \omega^2 = \frac{F_0 \cos \delta}{\gamma_0} \quad (5)$$

The desired output of the forced-oscillation method is an estimate of the phase lag ($\delta = -\omega t_{\text{lag}}$) between the displacement of the model and the aerodynamic loading; the aerodynamic damping derivatives, by convention, are then the negative of the damping constant C . Thus, by accurately measuring the time delay, the forced-oscillation method permits estimates of the damping derivatives; however, due to the low amplitudes of recorded signals, some postprocessing is required and is discussed in Sec. II.D.

C. Data Acquisition and Testing Procedure

To collect sufficient data to provide reliable estimates of the damping derivatives, a large number of oscillations are prescribed with which to estimate the time lag. Models are mounted at a particular incidence of angles of attack and sideslip, and are prescribed oscillations lasting for a record of 40 periods at frequencies of $f = 0.5, 1, 1.5, 2.0, 2.5,$ and 3.0 Hz; these values are similar to reported magnitudes of steady-state periodic in-flight motions of MAVs [47]. The physical frequencies are used to compute reduced frequencies of $k = fb/2U_0$, which permits a nondimensional comparison between different experimental setups. Data are sampled at $f_s = 1000$ Hz.

The time lags between the aerodynamic loads and the model displacement, measured with the microloading technology (MLT) force balance and encoders on each motor axis, respectively, are then computed at every zero crossing. Displacement amplitudes are 1 deg for pitch and yaw, 3 deg for roll, and 0.5 cm for plunge; the small-amplitude oscillations keep the loads within a linear regime, and smaller perturbations are possible for pitch and yaw due to the gearing on the MPS. While the forced-oscillation amplitudes must remain small to satisfy Eq. (1), it is not sufficient to assume that the aerodynamic damping of LAR wings is constant for any incidence angle relative to the freestream; thus, the small-amplitude tests are repeated at angles of attack of $\alpha = 0, 10, 20, 30, 40,$ and 50 deg, and corresponding sideslip angles of $\beta = 0, 10, 20,$ and 35 deg. This permits piecewise interpolations of the damping derivatives in flight dynamic simulations of the nonlinear equations of motion. The experiment is repeated to collect up to 10 records of each frequency and incidence-angle combination to ensure repeatability; the estimated time delays are then averaged over the records, and used to compute the relevant derivative.

D. Data Reduction

Acceptable measurements of t_{lag} require addressing issues of low signal-to-noise ratio (SNR), synchronizing data acquisition (DAQ) with specific points in the motion trajectory and precise filtering of the data. These issues will be briefly discussed in this section, and have been analyzed in greater detail in a previous work by the authors [29].

1. Motion Quality and Data-Acquisition Synchronization

The optical encoders used for position feedback control on the MPS motors are used to both track the desired motion of the axis and synchronize the beginning of DAQ. When the encoder on the axis of motion registers the beginning of the first step, the motion controller triggers a breakpoint, which is sent to the DAQ card and initiates the data acquisition. Figure 2 shows the measured encoder position for a given forced oscillation in pitch of $\theta_0 = 1$ deg at a frequency of 1 Hz; only the first five periods are shown for clarity. The discretized steps of the motor are seen to smoothly track the desired trajectory, permitting the use of Eq. (1) to describe the motion. To correlate the ground truth of the model with the rotation of the motor, high-speed camera videos were taken of the oscillating wing, and the time history of its angular displacement was matched with the encoder signal. This video also confirmed that motion occurred in only one degree of freedom, that is, during a prescribed pitch oscillation, the sideslip angle of the model did not vary.

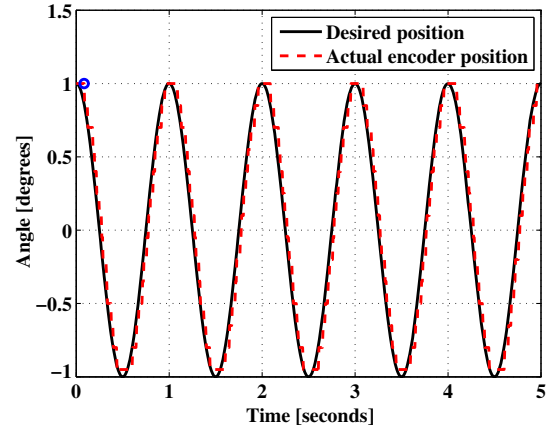


Fig. 2 Encoder measurements for a forced pitch oscillation; $f = 1$ Hz, $\theta_0 = 1$ deg.

2. Filtering Techniques

While the displacement of the model can be tracked by the motor encoders, the low amplitudes of oscillation and vibrational noise of the tunnel and MPS deteriorate the SNR of the data; often, the SNR is as low as 0.1. In many scenarios, this would be detrimental to the prospects of extracting viable data from the signal; however, an examination of the frequency content of the signals for all six channels of the MLT balance indicates that the vibrational noise typically occurs above 10 Hz, whereas the maximum motion frequency tested is 3 Hz. This small but significant bandwidth permits a low-pass filter to be set at a carefully selected cutoff frequency f_c , which removes the noise from the raw data without attenuating the desired component; for the frequencies between 0.5 and 3 Hz tested in this study, f_c was set between 3 and 5 Hz. Figure 3 shows the frequency content and the corresponding filter characteristics for a sample case of pitch motion occurring at $f = 1$ Hz.

While the gain properties of the filter must be carefully selected to attenuate the noise in the data, it is also important to recognize that the filter dynamics will impart a phase lag to the output signal; as the lag of the aerodynamic loading relative to the model displacement is the desired result of the experiment, this is a potential error source. To address this, a zero-phase filtering technique is used with the fourth-order Butterworth filter depicted in Fig. 3b. This method filters the signal in the forward direction, and then reverses the data array and performs the same filtering operation, eliminating the phase lag.

3. Validation of Algorithm

To ensure that the filtering techniques described in the previous section achieve the desired result, a test function was assigned a phase lag corresponding to $t_{\text{lag}} = 0.01$ s, and then contaminated with Gaussian noise and run through the postprocessing code used to compute the damping derivatives. An initial function γ_w , representing the motion of the wing, and a delayed function $\gamma_{w,\text{lag}}$, representing the loading, are defined:

$$\begin{aligned} \gamma_w &= A \sin(2\pi ft) \\ \gamma_{w,\text{lag}} &= A \sin(2\pi ft - \delta) \end{aligned} \quad (6)$$

Gaussian noise is then added to the data signal to create an SNR of 0.1; both full-spectrum (white noise) and band-limited noise signals are considered to determine how the presence of noise at the carrier frequency of $f = 2.5$ Hz affects the estimation of the time delays. The low-pass-filter cutoff frequency is nominally set at 4 Hz. Plots of the original signal, the frequency content of the band-limited noise, and the filtered signal are shown in Fig. 4; the imparted time delays are correctly measured to be 0.01 s with 95% confidence bounds on the order of $1e - 5$ [29]. The results indicate that zero-phase filtering satisfactorily eliminates the noise from the data, and estimates the time delays with a high degree of confidence; the presence of noise at the carrier frequency reduces the effectiveness of the filter, and the

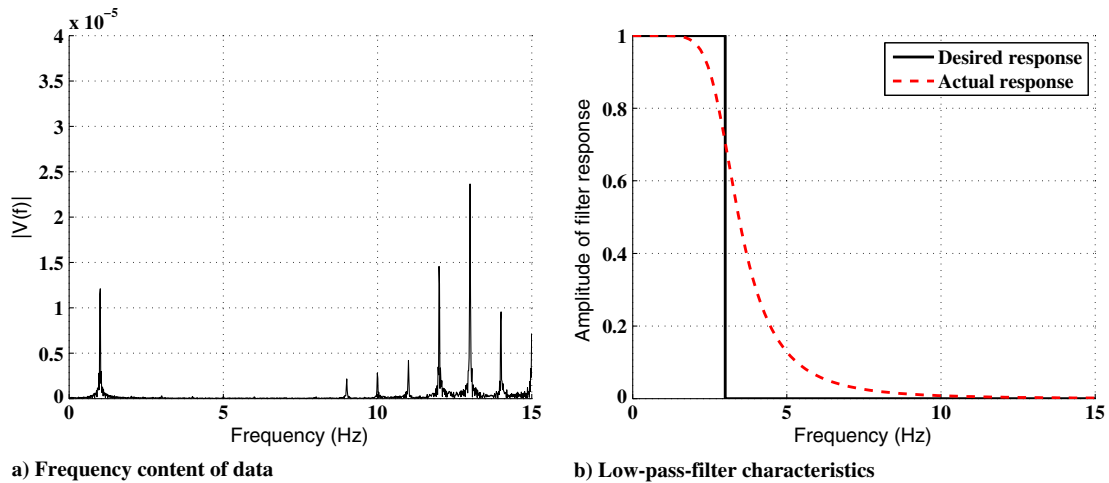


Fig. 3 Bandgap requirements for data postprocessing at $f = 1$ Hz.

use of a unidirectional filter imparts a significant lag to the measured data. The success of the zero-phase filter indicates that the phase lag of the experimental data can be computed with confidence, provided that the minimum noise frequency is a factor of 2–3 Hz higher than the motion carrier frequency.

III. Measured Damping Derivatives

The results presented in Sec. II.D indicate that it is possible to extract meaningful and reliable estimates of the aerodynamic

damping derivatives. A large test matrix was devised, and damping derivatives were computed for loads with dependencies on roll rate, pitch rate, and yaw rate ($\partial/\partial p$, $\partial/\partial q$, $\partial/\partial r$, respectively); derivatives due to translational accelerations, $\partial/\partial \dot{\alpha}$ and $\partial/\partial \dot{\beta}$, were found to be negligible. The results for oscillations in a given degree of freedom are plotted in Figs. 5–7 for the $\mathcal{R} = 1$ wing tested at a Reynolds number of 7.5×10^4 . Any load that demonstrated nonnegligible damping is listed on the horizontal axis, with the corresponding derivative on the vertical axis. In the figures, “xx” is used as a placeholder to denote normal (NF) and side (SF) forces as well as roll (RM), pitch (PM) and

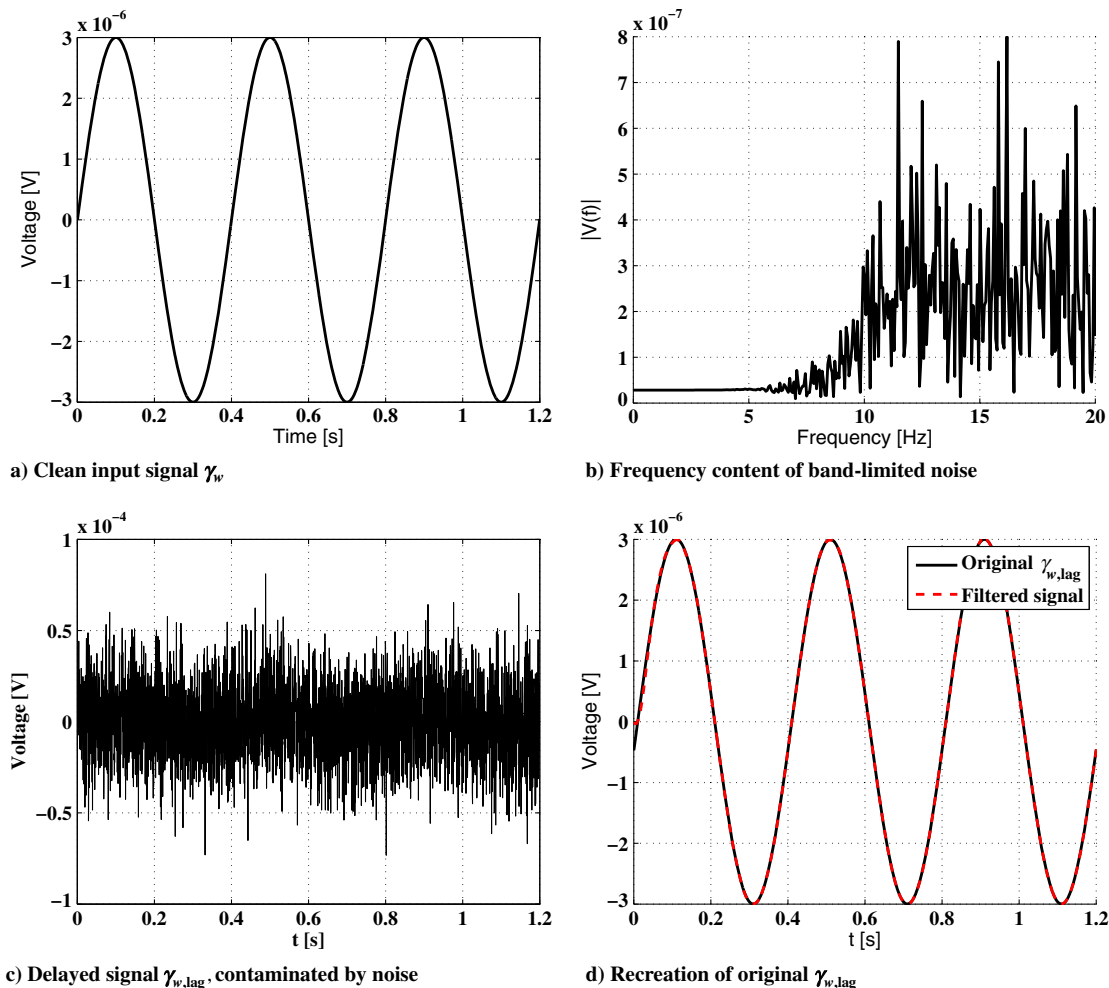


Fig. 4 Filtering validation results for test signal with $\text{SNR} = 0.01$.

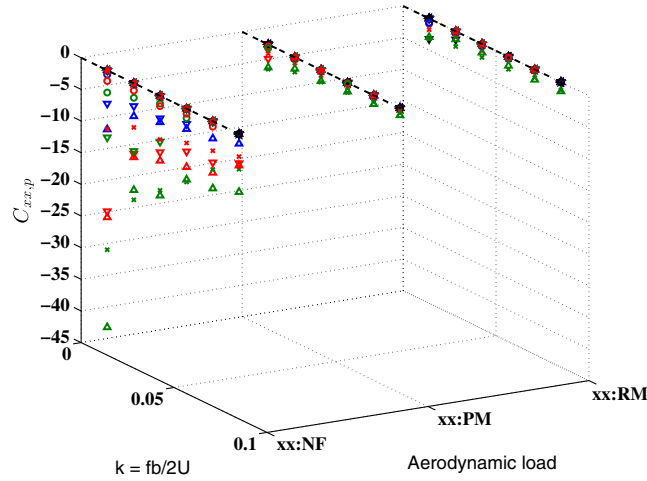


Fig. 5 Nondimensional $\partial/\partial p$ derivatives for an $R = 1$ wing at $Re = 7.5 \times 10^4$; $f = 0.5, 1, 1.5, 2, 2.5, 3$ Hz, $\alpha = 0$ deg (\circ), 10 deg (\times), 20 deg (\triangle), 30 deg (∇), 40 deg (\triangleleft), 50 deg (\diamond), $\beta = 0$ deg (black), 10 deg (blue), 20 deg (red), 35 deg (green). Color available online.

yaw (YM) moments. As previously published results have indicated that nondimensional aerodynamic loads do not vary significantly between Reynolds numbers of 1×10^4 and 1×10^5 for LAR wings, only a single representative condition was tested in this experiment to limit the amount of data being presented [17,19]. The results are presented in body axes (normal force and axial force) instead of stability axes (lift and drag) to avoid confusion between the lift force and roll moment, which are both often represented by the variable L .

The results displayed in Figs. 5–7 represent the first experimental measurements of the aerodynamic damping derivatives of LAR wings at low Reynolds numbers. The largest magnitudes are seen to be the damping of normal force in pitch ($C_{z,q}$), which are nominally an order of magnitude larger than any other derivative measured; however, the trends present for all derivatives are similar. The magnitudes of the damping derivatives are largest at the lowest oscillation frequencies, and decrease exponentially with higher values of k . The behavior of the data suggests that the aerodynamic damping approaches zero for $f > 3$ Hz ($k > 0.1$), although this is merely speculative, as experimental measurements are not currently feasible with the MPS at higher frequencies; however, a linear stability analysis of the LAR wing response presented in the following section indicates that the natural frequency of the inherent modes is around $f = 1$ Hz, in which the damping derivatives are well represented. All aerodynamic derivatives measured were negative,

implying positive (stable) damping. Some cross-coupled derivatives were observed, specifically damping in roll moment with pitch ($C_{L,q}$) and damping in normal force/pitch moment with roll rate ($C_{z,p}$ and $C_{M,p}$) at increased sideslip angles, although the magnitudes were typically small. Additionally, the roll damping derivative $C_{L,p}$ was conspicuously absent when no sideslip angle was present; this surprising result is attributed to the small wingspans of the LAR wing experiencing only minor variations in induced velocity due to the roll rate. The lack of roll damping is a plausible explanation for the jittery nature of MAV flight.

The damping derivatives of flat-plate wings with aspect ratios of 1.5 and 2 were also measured and were typically found to demonstrate the same trends as the $R = 1$ case. The maximum damping was present at $f = 0.5$ Hz, and decreases at greater motion frequencies. Most results indicated positive (stable) damping, although the normal force derivative due to roll rate $C_{z,p}$ was found to experience slight negative damping at the highest sideslip angles tested for $R = 2$. The most significant difference between the aspect ratios was a minor reduction in amplitude as the wingspan was increased, and the effects of the tip vortices on the loading were diminished. The close similarity of the results indicates that dynamic loading of these wings is affected in much the same way as the $R = 1$ case, which is also the case for the static loading [20]; as a result, only simulation results for an aspect ratio of unity are presented in this

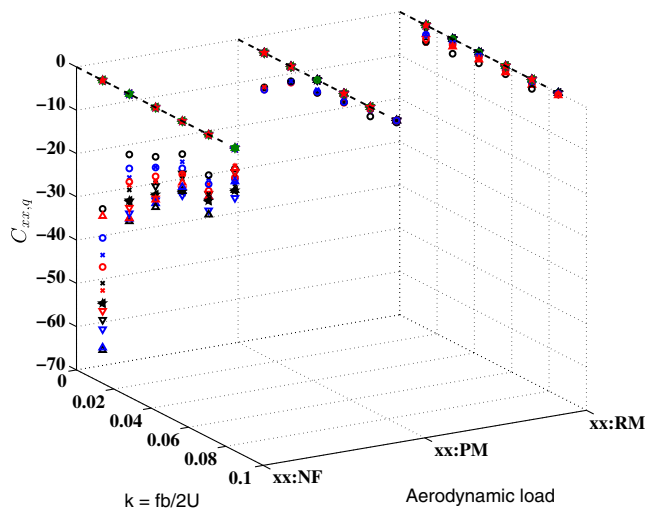


Fig. 6 Nondimensional $\partial/\partial q$ derivatives for an $R = 1$ wing at $Re = 7.5 \times 10^4$; $f = 0.5, 1, 1.5, 2, 2.5,$ and 3 Hz, $\alpha = 0$ deg (\circ), 10 deg (\times), 20 deg (\triangle), 30 deg (∇), 40 deg (\triangleleft), 50 deg (\diamond), $\beta = 0$ deg (black), 10 deg (blue), 20 deg (red), 35 deg (green). Color available online.

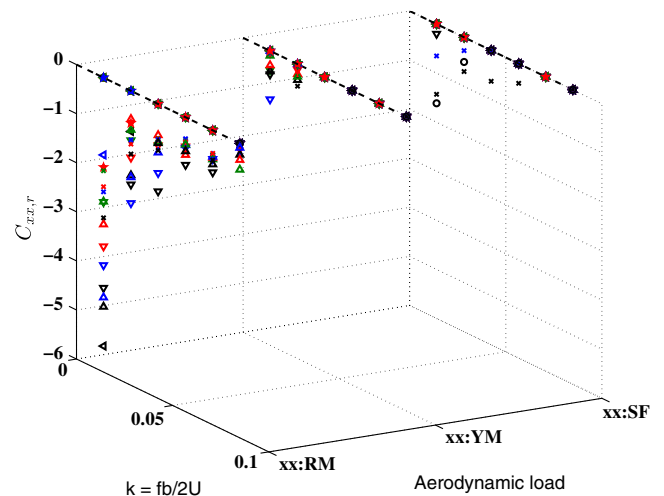


Fig. 7 Nondimensional $\partial/\partial r$ derivatives for an $R = 1$ wing at $Re = 7.5 \times 10^4$; $f = 0.5, 1, 1.5, 2, 2.5, 3$ Hz, $\alpha = 0$ deg (\circ), 10 deg (\times), 20 deg (\triangle), 30 deg (∇), 40 deg (\triangleleft), 50 deg (\diamond), $\beta = 0$ deg (black), 10 deg (blue), 20 deg (red), 35 deg (green). Color available online.

paper. They are representative of the stability characteristics of rectangular wings with $\mathcal{R} < 3$ for which roll stall is prevalent.

IV. Stability Considerations for LAR Wings

Previous publications by the authors and others have detailed the static loading characteristics of LAR wings [8,17–20]; the results from this investigation have provided the relevant damping derivatives for a wide variety of conceivable incidence angles. This makes it possible to completely describe the functionality of the aerodynamic loading, which permits the formulation of a dynamic model for LAR wings at low Reynolds numbers and an analysis of the modal response to perturbations from equilibrium flight. It will be shown that the unique loading conditions generated by the short wingspan, particularly the effects of roll stall on the roll and yaw moments of the wing, create a purely aerodynamic lateral-stability mode; furthermore, this mode can be shown to depend on angle of attack perturbations, indicating a cross coupling of the stability axes. Experimental data have shown that roll stall is present and significant for rectangular and tapered flat-plate wings, as well as for an MAV wing and complete MAV aircraft [20,21]; because of this, the canonical results discussed in the following sections for a flat plate with an aspect ratio of unity may be considered to represent a more general case for planforms that are affected by roll stall. Although no data are presented here for full airframes, the susceptibility of MAVs to roll stall indicates that their stability properties may be significantly impacted by the following results.

A. Longitudinal Instability

Before considering the lateral response of LAR wings to disturbances from equilibrium, the nature of longitudinal stability should be discussed. Symmetric wings of any aspect ratio are passively unstable in pitch, as it is not possible to obtain a negative (restoring) pitch stability derivative and a statically trimmed wing without either a horizontal tail or cambered/reflexed airfoil providing balanced moments [27]. Thus, solutions to the equations of motion will be dominated by the pitch instability and will not accurately portray the lateral dynamics; furthermore, simply fixing a constant angle of attack will eliminate any potential dependencies on longitudinal motion, which are expected to be significant due to the magnitude of the roll stall derivatives.

It is of interest in this investigation to analyze both the purely lateral modes (constant α) created by roll stall, and to also determine how the cross-coupled loads and nonlinear terms in the equations of motion affect the wing dynamics. To address this, angle of attack trajectories are prescribed in the solution instead of being implicitly solved for. In a physical sense, this may be considered to correspond to a time-varying vertical gust or a longitudinal short-period mode experienced by the flying wing. The prescribed angle of attack trajectories are given in Eq. (7):

$$\begin{aligned}\alpha(t) &= \alpha_0 \\ \alpha(t) &= \pm A \sin(\omega_\alpha t + \delta) + \alpha_0\end{aligned}\quad (7)$$

Finally, it should be noted here that the prescribed trajectory assumes that the subsequent variations in lateral loading do not affect the longitudinal motion of the wing. This is reasonable, as previously published static results [19] and the currently presented damping derivatives indicate typically negligible effects on longitudinal loading by lateral perturbations. With the procedure for addressing the longitudinal motion of the wing now defined, the equations of motion can be considered and simplified based on the experimentally determined loading regime.

B. Nonlinear Equations of Motion and Aerodynamic Load Dependencies

The system of coupled, nonlinear, first-order differential equations, which represent the evolution of the body-axis forces and moments of a rotating rigid body, are given in Eqs. (8) and (9):

$$\begin{Bmatrix} X \\ Y \\ Z \end{Bmatrix} = m \begin{Bmatrix} \dot{u} \\ \dot{v} \\ \dot{w} \end{Bmatrix} + m \begin{bmatrix} qw - rv \\ ru - pw \\ pv - qu \end{bmatrix} + mg \begin{bmatrix} \sin \Theta \\ -\cos \Theta \sin \Phi \\ -\cos \Theta \cos \Phi \end{bmatrix}\quad (8)$$

$$\begin{Bmatrix} L \\ M \\ N \end{Bmatrix} = \begin{Bmatrix} I_x \dot{p} - I_{xz} \dot{r} \\ I_y \dot{q} \\ I_z \dot{r} - I_{xz} \dot{p} \end{Bmatrix} + \begin{bmatrix} qr(I_z - I_y) - pqI_{xz} \\ pr(I_x - I_z) + (p^2 - r^2)I_{xz} \\ pq(I_y - I_x) + qrI_{xz} \end{bmatrix}\quad (9)$$

in which m is the mass of the body; g is the gravitational acceleration; u , v , and w are the translational components of velocity; p , q , and r are the rotational components of velocity; X , Y , and Z and L , M , and N are the force and moment components about the body axes; I_x , I_y , and I_z are the moments of inertia about the body axes; and I_{xz} is the product of inertia about the x and z axes; due to symmetry about the x - z plane, $I_{yz} = 0$. This is a valid assumption for the LAR wings used in this investigation, as well as for conventional aircraft. Dotted terms indicate a time derivative. The nonlinear system can be written in a form suitable for numerical integration:

$$\begin{aligned}\dot{u} &= X/m - qw + rv - g(\sin \Theta) \\ \dot{v} &= Y/m - ru + pw + g(\cos \Theta)(\sin \Phi) \\ \dot{w} &= Z/m - pv + qu + g(\cos \Theta)(\cos \Phi) \\ \dot{p} &= \left(I_x - \frac{I_{xz}^2}{I_z}\right)^{-1} \left[L + \frac{I_{xz}}{I_z} N - qr \left(\frac{I_{xz}}{I_z} + I_z - I_y \right) \right. \\ &\quad \left. - pq \left(\frac{(I_y - I_x)I_{xz}}{I_z} - I_{xz} \right) \right] \\ \dot{q} &= \frac{1}{I_y} [M - pr(I_x - I_z) + (p^2 - r^2)I_{xz}] \\ \dot{r} &= \left(I_z - \frac{I_{xz}^2}{I_x}\right)^{-1} \left[N + \frac{I_{xz}}{I_x} L - pq \left(I_y - I_x - \frac{I_{xz}^2}{I_z} \right) \right. \\ &\quad \left. - qr \left(\frac{(I_z - I_y)I_{xz}}{I_x} + I_{xz} \right) \right]\end{aligned}\quad (10)$$

in which the x , y , and z weight vectors have been expressed in terms of the Euler angles Φ and Θ . The terms in Eq. (10) are influenced by the aerodynamic angles and rates of the wing; an accurate knowledge of the load dependencies is required for a correct model. The conventional Taylor series expansion of these loads is well known for high-aspect-ratio wings, and typically assumes that it is possible to decouple lateral and longitudinal axes [27]. Because of the significant differences in the associated flow regime, determining the dependencies of LAR wings requires experimental evidence, which considers potential cross-coupled loading and aerodynamic damping [19]. The expansions of X , Y , Z , and M about a zero sideslip angle are found to be nominally identical to high-aspect-ratio cases; however, the presence of roll stall and the associated α and β dependencies alter the nature of the L and N (roll and yaw moments) for an $\mathcal{R} = 1$ wing:

$$\begin{aligned}\Delta L &= \frac{\partial L}{\partial \beta} \Delta \beta + \frac{\partial L}{\partial \alpha} \Delta \alpha + \frac{\partial L}{\partial p} \Delta p + \frac{\partial L}{\partial q} \Delta q + \frac{\partial L}{\partial r} \Delta r \\ \Delta N &= \frac{\partial N}{\partial \beta} \Delta \beta + \frac{\partial N}{\partial \alpha} \Delta \alpha + \frac{\partial N}{\partial r} \Delta r\end{aligned}\quad (11)$$

It may be noted in Eq. (11) that expected lateral derivatives, such as the yaw-moment dependence on roll rate ($\partial N / \partial p$), are not included, as the experimental data from forced-oscillation testing indicated that these values were negligible for LAR wings. Of most significant interest in Eq. (11) is the presence of the cross-coupled derivatives $\partial L / \partial \alpha$ and $\partial N / \partial \alpha$, which couples the evolution of the lateral moments to variations in angle of attack. As the models tested to obtain these experimental dependencies were simple flat-plate, rectangular wings, these derivatives are created purely due to the aerodynamic loading of LAR wings. When the aspect ratio is increased to 3, $\partial N / \partial \alpha$ disappears and $\partial L / \partial \alpha$ is significantly reduced

[20]; this indicates the unique aerodynamic regime of LAR wings, and suggests the possibility of stability modes, which are specific to this type of vehicle.

A final simplification to the equations of motion is achieved by constraining the pitch angle to be constant; therefore, in addition to the \dot{u} and \dot{w} equations of Eq. (10) being explicitly defined in terms of the prescribed $\alpha(t)$ trajectory, the pitch-rate equation \dot{q} is equal to zero. Thus, all cross coupling due to longitudinal variations is due to the varying vertical velocity as opposed to coupled perturbations of angles of attack and pitch. Furthermore, for flat-plate wings, the cross product of inertia I_{xz} is negligible. These simplifications reduce the equations of motion to a more manageable form:

$$\begin{aligned}\dot{u} &= U_0 \cos[\alpha(t)] \\ \dot{v} &= Y/m - ru + pw + g(\cos \Theta)(\sin \Phi) \\ \dot{w} &= U_0 \sin[\alpha(t)] \\ \dot{p} &= \Delta L/I_x \\ \dot{q} &= 0 \\ \dot{r} &= \Delta N/I_z\end{aligned}\quad (12)$$

The Euler angles Φ , Θ , and Ψ are defined in the usual way. Numerically integrating these equations for a prescribed longitudinal trajectory of $\alpha(t)$ and a given lateral perturbation (Δv , $\Delta \phi$, Δp , Δr) yields the time histories of the lateral state variables, and can be used to identify stability modes created by the influence of roll stall on the wing aerodynamics. In the following sections, the nonlinear solutions of Eq. (12) are considered to be the most accurate representations of the response of the wing, as they are based upon instantaneous values of the experimentally obtained forces and moments, and do not require approximations of the gravitational or nonlinear terms in the side-force equation. Linear models that compare favorably with the nonlinear results are desirable, as they then permit straightforward interpretations of the stability characteristics of the wing. Finally, it should be noted here that, although the integration is carried out in the body axes of the wing (u , v , w), the results will be presented in the more conventional stability axes, in which

$$\begin{aligned}\alpha &= \tan^{-1}\left(\frac{w}{u}\right) \\ \beta &= \sin^{-1}\left(\frac{v}{U}\right)\end{aligned}\quad (13)$$

C. Linearized Models of LAR Modes

A linearized model can be developed from the nonlinear equations of motion in Eqs. (8) and (9) by assuming that the Euler-angle perturbations are small; that the wing is an $\mathcal{R} = 1$ flat plate, in which $I_{xz} = 0$ and $I_x = I_y$; that the initial values of side force and roll, yaw, and pitch moments are zero; and that the products of rates (qr , pr) are negligible. It should be noted that the pw term in the side-force equation is retained due to the potentially high roll rates associated with LAR wings, although it is typically ignored for conventional aircraft. It is linearized about the initial vertical-velocity component, such that $pw = pw_0$. The final linear equations of motion become

$$\begin{aligned}\Delta X - mg \cos \Theta_0 \theta &= m(\dot{u} + qw_0) \\ \Delta Y + mg \cos \Theta_0 \phi &= m(\dot{v} + rU_0 - pw_0) \\ \Delta Z - mg \sin \Theta_0 \theta &= m(\dot{w} - qU_0) \\ \Delta L &= I_x \dot{p} \\ \Delta M &= I_y \dot{q} \\ \Delta N &= I_z \dot{r}\end{aligned}\quad (14)$$

in which the Δ terms represent the force and moment perturbations from equilibrium. These terms can be expanded using a Taylor series,

and a linear system for the response of the wing can be constructed. The dependencies of Eq. (11) are incorporated into Eq. (14); the roll moment due to pitch rate $\partial L/\partial q$ is neglected, as q is constrained to be zero. The ensuing linearized system is defined in Eq. (15):

$$\begin{aligned}\begin{bmatrix} 1 & 0 & 0 & 0 & 0 & 0 \\ 0 & 1 & 0 & 0 & 0 & 0 \\ 0 & 0 & mU_0 & 0 & 0 & 0 \\ 0 & 0 & 0 & 1 & 0 & 0 \\ 0 & 0 & 0 & 0 & I_x & 0 \\ 0 & 0 & 0 & 0 & 0 & I_z \end{bmatrix} \begin{Bmatrix} \ddot{\alpha} \\ \dot{\alpha} \\ \dot{\beta} \\ \dot{\phi} \\ \dot{p} \\ \dot{r} \end{Bmatrix} \\ = \begin{bmatrix} 0 & -\omega_\alpha^2 & 0 & 0 & 0 & 0 \\ 1 & 0 & 0 & 0 & 0 & 0 \\ 0 & Y_\alpha & Y_\beta & mg \cos \Theta_0 & mw_0 & -mU_0 \\ 0 & 0 & 0 & 0 & 1 & 0 \\ 0 & L_\alpha & L_\beta & 0 & L_p & L_r \\ 0 & N_\alpha & N_\beta & 0 & 0 & 0 \end{bmatrix} \begin{Bmatrix} \alpha \\ \beta \\ \phi \\ p \\ r \end{Bmatrix}\end{aligned}\quad (15)$$

in which the first two equations ($\ddot{\alpha}$ and $\dot{\alpha}$) are artificially constructed to induce a sinusoidal variation in angle of attack corresponding to Eq. (7). Stability derivatives are presented in dimensional form so that the solution to Eq. (15) produces time histories of the state variables in physical units.

It is apparent that a number of stability derivatives, which commonly occur in conventional aircraft analysis, such as Y_r , Y_p , N_p , and N_r , are not present in Eq. (15). This is based upon the experimental results presented in Sec. III, which indicate that the yaw or roll rotations (r or p , respectively) did not generate a periodic load in the side force or yaw moment (Y or N). In a conventional aircraft, these derivatives are typically associated with the roll–yaw coupling created by the vertical tail [27]; unlike roll stall, which was still found to be prevalent due to the LAR flow regime, these loads were experimentally found to be insignificant for the canonical flat-plate wing. The L_p derivative is retained in Eq. (15), as the results shown in Fig. 5 indicate that it is present, albeit with small magnitude, for high sideslip angles ($\beta \geq 20$ deg). L_r was shown to be present in Fig. 7 for a number of incidence angles, although, again, the dimensionalized magnitude is small relative to L_β , and will not greatly affect the dynamics of the system.

The simplified nonlinear equations of motion and the linearized system of equations presented in Eqs. (12) and (15), respectively, are solved for the time histories of the lateral state variables:

$$\mathbf{x}_{\text{lat}} = \{\beta \quad \phi \quad p \quad r\}^T \quad (16)$$

The accuracy of the linear model in representing the nonlinear equations of motion is assessed, and the nature of the wing response is discussed and quantified. Initially, the angle of attack is held constant to determine the pure lateral response in Sec. IV.D; the sinusoidal trajectory of Eq. (7) is then prescribed, and the ensuing effects on the modal response of the wing are discussed in Secs. IV.E and IV.F.

D. Purely Lateral Motion

The initial-condition response of the system of equations described in Eq. (15) is evaluated for equilibrium angles of $\alpha_0 = 5$ and 15 deg, $\beta_0 = 0$ deg, and an arbitrary lateral perturbation of $\mathbf{x}_{\text{lat},0} = \{1 \text{ deg} \quad 0 \quad 0 \quad 0\}^T$. The results shown in Figs. 8 and 9 demonstrate the development of a periodic, divergent mode. Despite the large magnitudes of the perturbations, which would seem to invalidate several assumptions made in the linearization process, the nonlinear equations are matched nicely for as much as 3 s of motion.

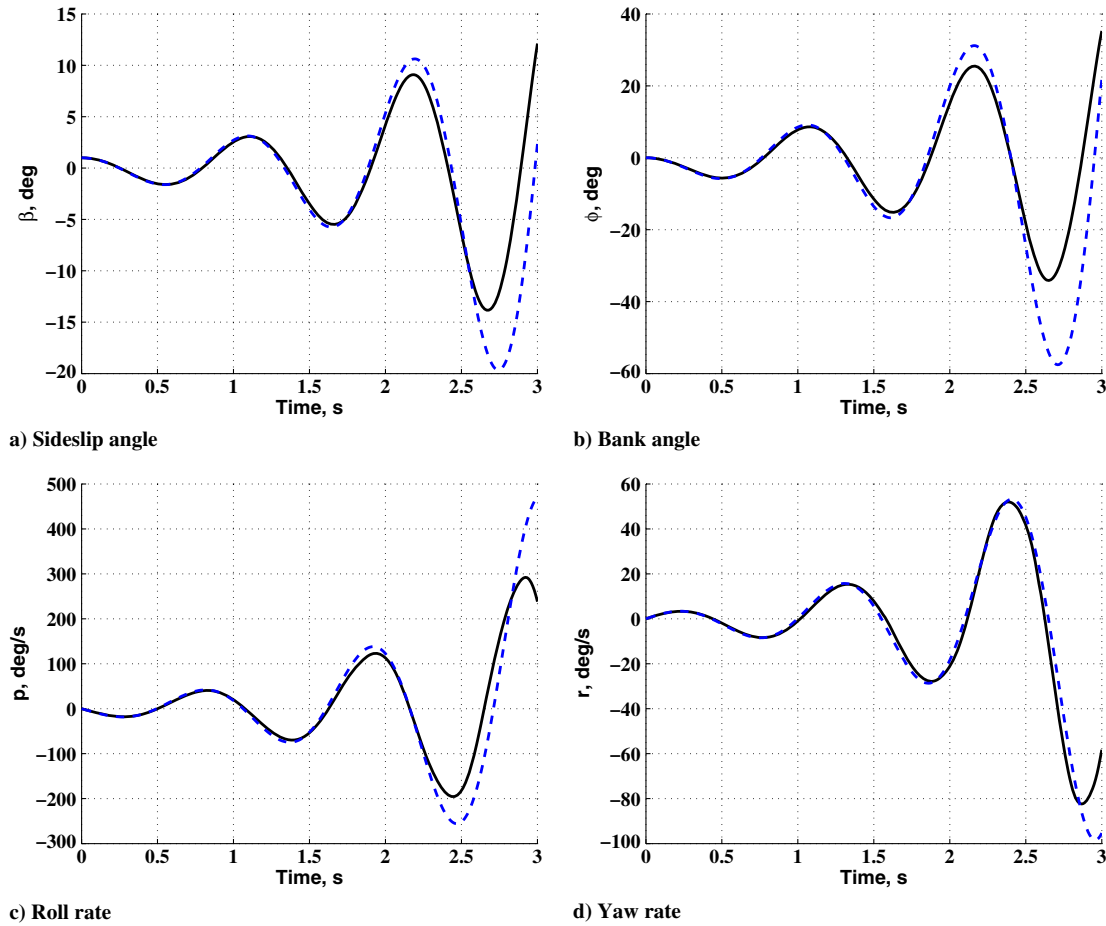


Fig. 8 Comparison of nonlinear (solid line) and linear (dashed line) response; $\alpha_0 = 5$ deg, $\beta_0 = 0$ deg.

As such, the results of a linear analysis can accurately predict the stability characteristics of the wing. The parameters of the mode shapes computed from solving the eigenvalue problem, including the eigenvalues λ and eigenvectors v , normalized magnitude and phasing of the state variables, and the damping ζ and undamped natural frequencies of periodic lateral modes ($\omega_{n,lat}$), are listed in Table 1.

As seen in the simulation results, a divergent and oscillatory mode exists with significant participation by all four variables. The largest contribution is due to the roll rate, which is driven by large moments created by roll stall and corresponding low moments of inertia about the x axis. The relative magnitudes and phase delays between the variables approximately correspond with those expected for the Dutch roll of a conventional aircraft [28]. The undamped natural frequencies are all below $\omega_{n,lat} = 10.2$ rad/s [$f = 1.6$ Hz], which places them within the range of frequencies at which the damping derivatives were measured experimentally.

In essence, these results demonstrate how the loading created by roll stall — predominantly the large magnitude of the roll moment due to sideslip L_β — induces a linear, but divergent, Dutch-roll-type mode inherent to LAR wings. The oscillatory and unstable results of Figs. 8 and 9, computed for an arbitrary initial condition $\mathbf{x}_{lat,0}$, which does not specifically excite any of the modes listed in Table 1, indicate that this mode dominates the response of the wing even for small sideslip perturbations. This is confirmed by considering the response of the state variables to initial conditions which produce the mode, computed as the real part of the normalized complex eigenvector from Table 1; this response is plotted in Fig. 10 for $\alpha_0 = 15$ deg, and is seen to closely resemble the response to the arbitrary initial condition of Fig. 9. Although the amplitude of oscillations increases, resulting in a less effective linear approximation, the similarity of the plots indicates that the lateral response of LAR

wings is dominated by the divergent harmonic behavior of this unstable Dutch-roll mode.

The second set of eigenvalues present for both values of the equilibrium angle of attack in Table 1 represents an overdamped, stable mode, which is also experienced by LAR wings. The response of variables returns to the equilibrium value typically within 1 s, and no harmonic oscillations are observed; the mode is excited by large initial bank angles, which are mostly out of phase with the sideslip angle. Unlike conventional aircraft, which exhibit roll sustenance and spiral modes, LAR wings do not experience real modes instigated by roll stall. As this mode is passively heavily damped, it does not contribute to instabilities, and therefore, is not of great interest in the scope of this study.

E. Effects of Angle of Attack Perturbations: The Roll-Resonance Mode

Conventional formulations of the Dutch-roll mode assume that it is unaffected by the longitudinal motion of the aircraft; however, due to the loads created by roll stall for LAR wings, the roll and yaw moments exhibit a dependency on the angle of attack. Furthermore, the high values of p and r seen in Figs. 8–10 can cause the $p\omega$ and ru nonlinear terms to become significant in the side-force equation. A sinusoidal angle of attack trajectory of $\alpha(t) = A_0 \sin(\omega_\alpha t)$ is prescribed in the linear and nonlinear equations to investigate the effects on the response of the lateral variables. The amplitude is set to $A_0 = 3$ deg; while this is an arbitrary value, the results are found to be nominally identical for $A_0 \leq 5$ deg. Larger amplitudes will naturally affect the response of the state variables; however, the purpose of this study was to determine how small perturbations from equilibrium may initiate unstable modes. Hence, a small-amplitude oscillation is maintained. The frequency ω_α and phase δ of the angle of attack input are varied to assess the ensuring effects on the wing response; selected values of ω_α are based on the natural frequencies

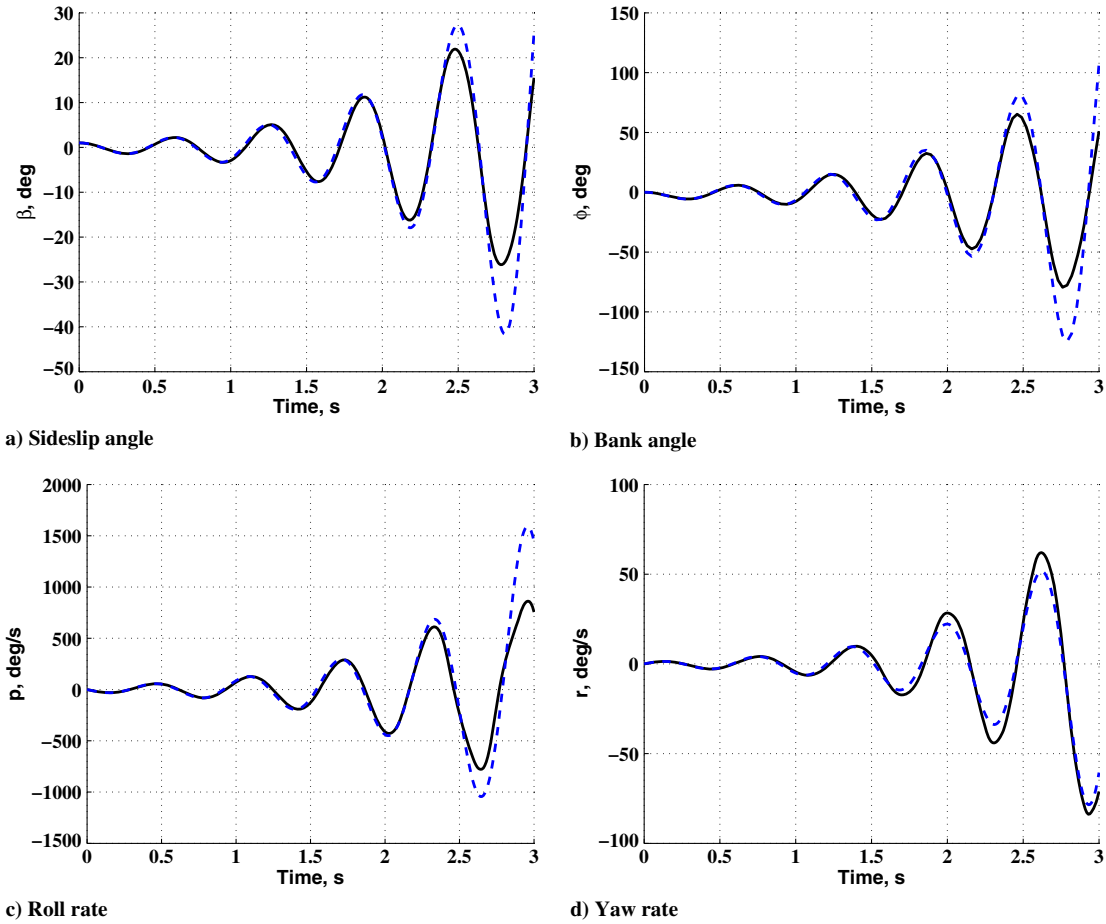


Fig. 9 Comparison of nonlinear (solid line) and linear (dashed line) response; $\alpha_0 = 15$ deg, $\beta_0 = 0$ deg.

of the lateral modes seen in Table 1, such that $\omega_\alpha/\omega_{n,lat} = 0.5, 1,$ and 2 . The linear equations are trimmed about $\alpha_0 = 5$ deg and $\beta_0 = 5$ deg; the nonzero trim sideslip angle is used so that the cross-coupled roll-stall derivatives $Y_\alpha, L_\alpha,$ and N_α are also nonzero. The time histories of the state variables for these test parameters are displayed in Fig. 11.

The results of these simulations indicate that the presence of longitudinal perturbations does affect the response of all four lateral variables, although the constraint that the amplitude of the angle of attack variations remains small causes only subtle effects in most cases. The additional restoring forces and moments attributed to L_α

and N_α increase the frequency and the magnitude of the response relative to the pure lateral cases of Figs. 8–10. The linearized model provides a reasonable approximation for the trajectory of the wing for angle of attack variations at frequencies of $\omega_\alpha/\omega_{n,lat} = 0.5$ and 2 . While some overshoot is present at higher sideslip deflections where the values for the stability derivatives computed at a trim condition of $\beta_0 = 5$ deg are no longer valid, the main features of the response are correctly captured.

When the frequency of $\alpha(t)$ is equal to the natural frequency of the lateral response, however, it is clear that the linear time-invariant (LTI) model of Eq. (15) breaks down. The most significant variation

Table 1 Parameters of lateral-stability modes at equilibrium angles of $\alpha_0 = 5$ and 15 deg

α, deg	λ	v	$ v $	δ, deg	ζ	$\omega_{n,lat}, \text{rad/s}$
5	$1.1 \pm 5.7i$	$\begin{Bmatrix} -0.0004 \pm 0.054i \\ 0.032 \pm 0.162i \\ 0.961 \\ -0.201 \pm 0.074i \end{Bmatrix}$	$\begin{Bmatrix} 0.057 \\ 0.172 \\ 1 \\ 0.223 \end{Bmatrix}$	$\begin{Bmatrix} -90 \\ -79 \\ 0 \\ -160 \end{Bmatrix}$	-0.192	5.82
	$-1.65 \pm 1.69i$	$\begin{Bmatrix} -0.022 \\ -0.261 \pm 0.266i \\ 0.881 \\ -0.114 \pm 0.268i \end{Bmatrix}$	$\begin{Bmatrix} 0.025 \\ 0.423 \\ 1 \\ 0.331 \end{Bmatrix}$	$\begin{Bmatrix} -359 \\ -134 \\ 0 \\ -113 \end{Bmatrix}$	0.699	2.37
15	$1.35 \pm 10.1i$	$\begin{Bmatrix} -0.002 \pm 0.032i \\ 0.013 \pm 0.097i \\ 0.993 \\ -0.049 \pm 0.012i \end{Bmatrix}$	$\begin{Bmatrix} 0.032 \\ 0.099 \\ 1 \\ 0.051 \end{Bmatrix}$	$\begin{Bmatrix} -94 \\ -82 \\ 0 \\ -167 \end{Bmatrix}$	-0.133	10.2
	$-2.33 \pm 9.73i$	$\begin{Bmatrix} 0.008 \pm 0.002i \\ -0.337 \pm 0.141i \\ 0.922 \\ -0.024 \pm 0.124i \end{Bmatrix}$	$\begin{Bmatrix} 0.009 \\ 0.396 \\ 1 \\ 0.138 \end{Bmatrix}$	$\begin{Bmatrix} 16 \\ -157 \\ 0 \\ -100 \end{Bmatrix}$	0.923	2.53

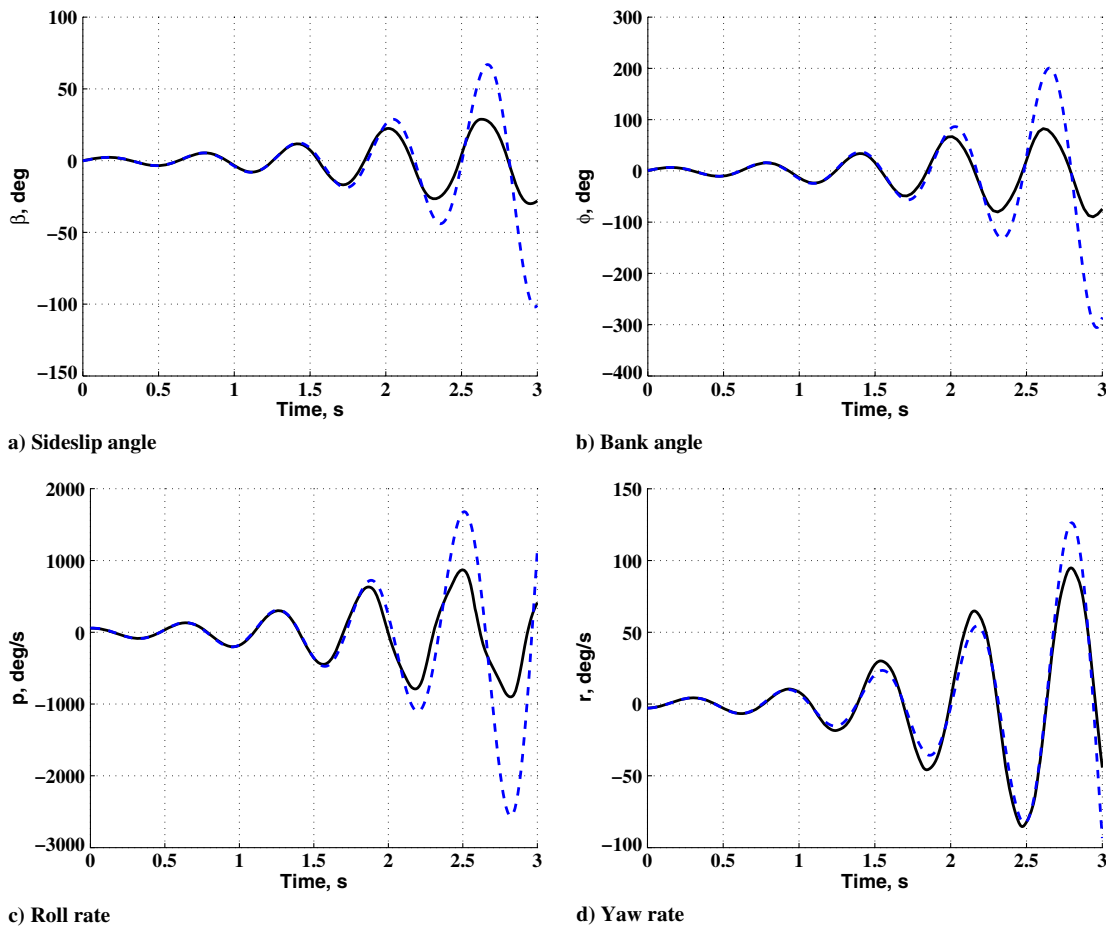


Fig. 10 Nonlinear (solid line) and linear (dashed line) response to divergent initial conditions; $\alpha_0 = 15$ deg, $\beta_0 = 0$ deg.

is that of the bank angle ϕ shown in Fig. 11e; the results of the nonlinear simulation do not oscillate about zero, but instead drift toward a considerable amplitude (-150 deg within the 3 s of the simulation). This behavior is only observed when ω_a is within 50% of the natural frequencies of the original lateral mode, and suggests that the relative phasing of $\alpha(t)$ and $\beta(t)$ in these cases causes a fundamental shift in the aerodynamic loading conditions, and resulting stability characteristics, of LAR wings. This description of the interactive effects of oscillations in angles of attack and sideslip on the bank-angle stability of LAR wings represents a mode which has not previously been described; furthermore, it is a mode that is seen to arise from small perturbations from an equilibrium flight condition. As the response of ϕ is highly dependent upon the frequencies of $\alpha(t)$ and $\beta(t)$ oscillations having similar values, this mode will be referred to herein as the *roll-resonance* mode.

A schematic depicting the development of the first two cycles of roll-resonance is shown in Fig. 12 for an initial perturbation, which excites the divergent lateral response ($r_0 < 0$ deg/s, $p_0 > 0$ deg/s); simultaneous views of the sideslip angle (with trailing tip vortices included), the bank angle from a downstream perspective, and the angle of attack are provided. The lateral displacement of the wing is not shown. Relative magnitudes of the angular displacements and rates are taken from the simulation results shown in Fig. 11. The effects of the angle of attack on the relative tip-vortex strength are included, and significantly influence the roll-resonance. The maxima and minima of the angle of attack trajectory are seen to coincide with the largest positive and negative values of the sideslip angle, respectively, in Figs. 12b, 12d, 12f, and 12h. At these yawed configurations, the trailing vortices are illustrated in the skewed distribution seen in the smoke-wire-visualization testing to which the linear relationship between the roll moment and the angle of attack was attributed [20]. Because of this flow asymmetry, at the positive sideslip displacements (Fig. 12b), roll stall causes the strength of the tip vortices to increase

with the angle of attack, and impart a greater-magnitude roll moment than would be generated by a wing at constant angle of attack. Similarly, during negative sideslip displacements (Fig. 12d), the lower angle of attack reduces the strength of the tip vortices and the associated restoring roll moment. As the wing continues to oscillate in sideslip due to a restoring yaw moment (also generated by the tip-vortex asymmetry of roll stall [20]), the disparity in tip-vortex strength and roll-moment magnitude perpetuates, and the bank angle of the wing is driven in the negative direction; while it still oscillates and may reach a less negative angle (Fig. 12f), it never returns to a wing-level configuration. It should be noted that, if the angle of attack does not change, the strength of the tip vortices also remains nominally constant, and the restoring roll moment remains in proportion with the sideslip angle; this results in the divergent Dutch-roll mode seen in Figs. 8–10.

F. Linear Time-Variant Model for Roll-Resonance

While the integration of Eq. (12) provides the full nonlinear response of the wing to a set of initial perturbation conditions, a more simplified model that provides more insight into the nature of the roll divergence is of interest. Because of the angle of attack variations that instigate the roll-resonance mode, a LTI model does not accurately capture the behavior of the system, as the stability derivatives of Eq. (15) will evolve with the instantaneous value of $\alpha(t)$; this much is seen in Fig. 11. Furthermore, the initial-condition response method commonly used to solve the linear system in Eq. (15) will not predict the departure in bank angle from equilibrium seen in Fig. 11e, as this technique inherently assumes a form of the solution e^{At} , which may oscillate about the origin, or smoothly grow or decay, but not both. These conditions suggest the need for a time-variant model, which accounts for variations in the stability derivatives with angle of attack. The state vector must be evaluated at every time step to capture the divergent nature of the bank angle. A linear time-variant (LTV) model is given by Eq. (17):

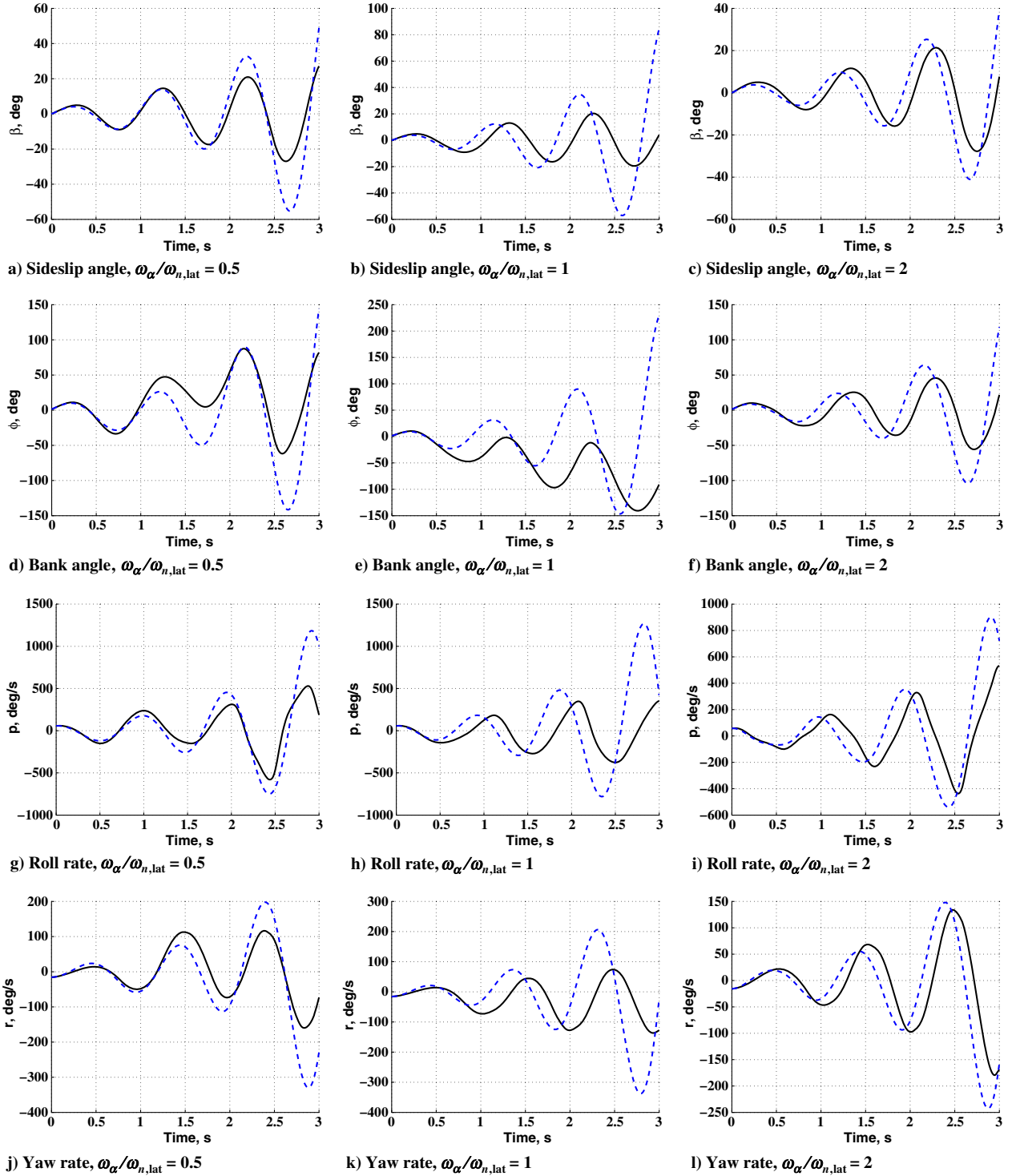


Fig. 11 Nonlinear (solid line) and linear (dashed line) response to divergent initial conditions; $\alpha_0 = 5$ deg, $\beta_0 = 5$ deg with $\alpha(t) = 3 \sin(\omega_\alpha t)$.

$$\begin{aligned}
 & \begin{bmatrix} mU_0 & 0 & 0 & 0 \\ 0 & 1 & 0 & 0 \\ 0 & 0 & I_x & 0 \\ 0 & 0 & 0 & I_z \end{bmatrix} \begin{Bmatrix} \dot{\beta} \\ \dot{\phi} \\ \dot{p} \\ \dot{r} \end{Bmatrix} \\
 & = \begin{bmatrix} Y_\beta & mg \cos \Theta_0 & mw_0 & -mU_0 \\ 0 & 0 & 1 & 0 \\ L_\beta(\alpha(t)) & 0 & L_p & L_r \\ N_\beta & 0 & 0 & 0 \end{bmatrix} \begin{Bmatrix} \beta \\ \phi \\ p \\ r \end{Bmatrix} \quad (17)
 \end{aligned}$$

This model differs from Eq. (15) by allowing the roll stability derivative L_β to vary with angle of attack and, implicitly, time. In addition, as the angle of attack variations are constrained to be ± 3 deg and are therefore typically smaller than the sideslip perturbations, the direct effects of the cross-coupled derivatives Y_α , L_α , and N_α are ignored. The results of the integrated LTV system are compared with the full nonlinear response for an input angle of attack frequency of $\omega_\alpha = \omega_{n,lat}$, and are compared with the state-variable responses of Figs. 11b, 11e, 11h, and 11k. The results are displayed in Fig. 13.

Relative to the LTI model of Eq. (15), the LTV model provides a better approximation of the behavior of the roll-resonance mode.

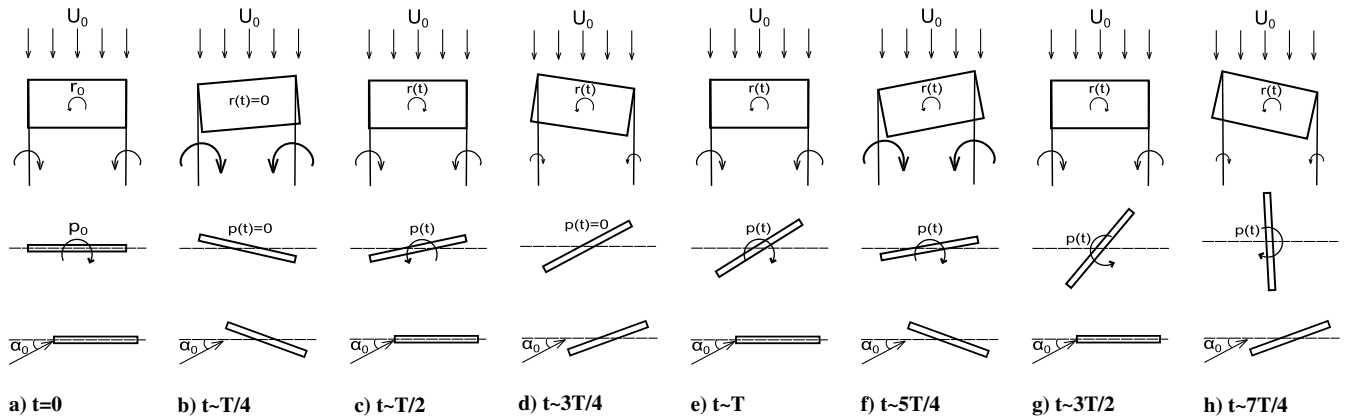


Fig. 12 Roll-resonance motion viewed from top, downstream, and side (rows 1–3, respectively).

Figure 13b depicts the response of the bank angle, in which the direction of the divergence, the amplitude and frequency of the oscillations, and the magnitude of the deviation from the equilibrium angle of $\phi_0 = 0$ deg are captured by the integration of Eq. (17). As the only stability derivative allowed to vary with time is L_β , it is clear that the effects of angle of attack perturbations on the roll stability derivative significantly impact the roll response of LAR wings; effects due to the cross-coupled derivatives would become significant for larger amplitude oscillations in $\alpha(t)$. This is the more quantitative explanation for the roll-resonance response illustrated in Fig. 12, as these relevant stability derivatives are attributed to the loading conditions created by the tip-vortex asymmetry of roll stall. When

exacerbated by the low I_x moments of inertia of LAR wings, this results in the divergent response of the bank angle. It is interesting to note that this behavior can still be modeled by a linear system, such as Eq. (17), although the value of L_β must be updated for even small variations in angle of attack ($\Delta\alpha \leq 3$ deg).

To compare the different linear approximations used in this paper, a normalized rms deviation (RMSD) is computed for the linear and nonlinear models using Eq. (18):

$$x_{\text{RMSD}} = \sqrt{\frac{1}{n} \sum_{i=1}^n \left(\frac{x_{\text{NL}}(i) - x_{\text{lin}}(i)}{|x_{\text{NL}}|_{\text{max}}} \right)^2} \quad (18)$$

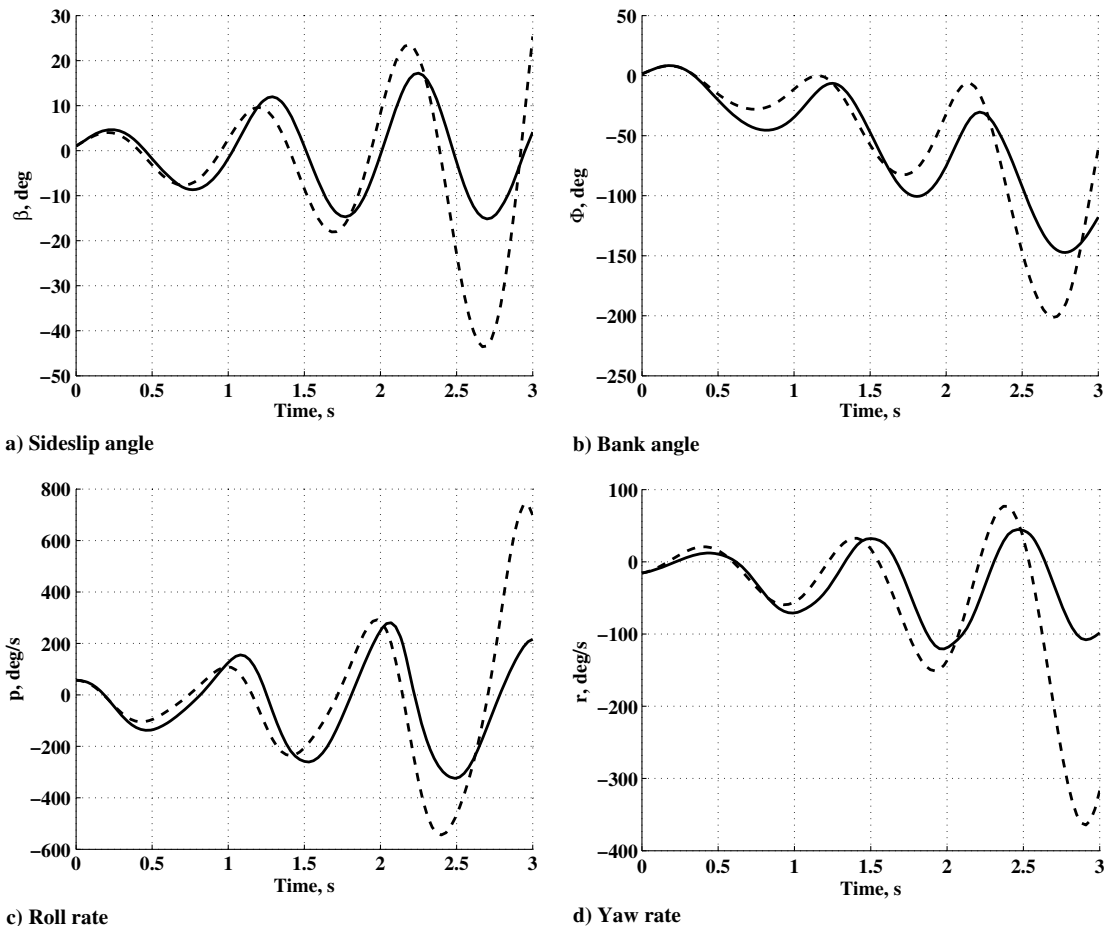


Fig. 13 Nonlinear (solid line) and LTV (dashed line) response to divergent initial conditions; $\alpha_0 = 5$ deg, $\beta_0 = 5$ deg, $\alpha(t) = 3 \sin(\omega_\alpha t)$, $\omega_\alpha/\omega_{n, \text{lat}} = 1$.

Table 2 Normalized RMSDs between linear models and nonlinear solutions

Case	α_0	β_0	$\frac{\omega_\alpha}{\omega_{n,lat}}$	Figures	$x_{\text{RMSD}}(t < 1)$				$x_{\text{RMSD}}(t < 3)$			
					β	ϕ	p	r	β	ϕ	p	r
Divergent Dutch roll	5	0	0	8	0.04	0.05	0.03	0.05	0.25	0.28	0.16	0.08
	15	0	0	9	0.05	0.05	0.08	0.07	0.15	0.16	0.20	0.05
Roll-resonance (LTI model)	5	5	0.5	11a, 11d, 11g, 11j	0.11	0.09	0.12	0.13	0.36	0.40	0.37	0.38
	5	5	1	11b, 11e, 11h, 11k	0.45	0.53	0.57	0.19	1.08	0.63	1.05	0.76
	5	5	2	11c, 11f, 11i, 11l	0.34	0.37	0.29	0.15	0.38	0.58	0.39	0.29
Roll-resonance (LTV model)	5	5	1	13	0.20	0.23	0.20	0.09	0.44	0.18	0.36	0.53

in which x_{NL} and x_{lin} are the nonlinear and linear responses, respectively. The value x_{RMSD} is normalized by the maximum value of the nonlinear solution over the domain of interest, so that the relative magnitudes of different variables may be compared. It was computed for the state variables of all simulation results presented in this paper for $0 < t < 1$ s and $0 < t < 3$ s to describe how the linear approximation degrades as the oscillation amplitude increases. The results are presented in Table 2, and typically corroborate the qualitative results obtained by observation. Roll-resonance is seen to increase the RMSD by an order of magnitude when the angle of attack oscillations occur at the natural frequency of the lateral mode ($\omega_\alpha/\omega_{n,lat} = 1$). The implementation of the LTV model, listed in the bottom row of Table 2, reduces the deviation between the linear and nonlinear models by over 50% for $t < 1$ s, and by around 75% over the entire 3 s duration of the simulation. Similar reductions are present for the other state variables, again indicating the better approximation of the LTV model.

G. Attenuation of the Roll-Resonance Mode

As both the divergent Dutch-roll and roll-resonance modes are found to be unstable even for small perturbations from equilibrium flight, it is desirable to determine a mechanism for mitigating these responses. A range of scaling factors is applied to L_β to determine the effects on the ensuing eigenvalues; the results are tabulated in Table 3. It can be seen that reducing the roll stability derivative by a factor of 1/11 produces positive real parts of the eigenvalues, and thus, drives the system stable, attenuating the divergent Dutch-roll mode; a larger scaling factor increases the magnitude of the negative real eigenvalue component, and thus, improves the stability characteristics. In a physical sense, the decreased impact of L_β on the instantaneous loading of the wing attenuates the roll moment generated by roll stall, and thus, reduces the unstable lateral response. It should be noted here that similar results are achieved by increasing the N_β derivative, also listed in Table 3, effectively stiffening the directional stability of the wing and preventing the sideslip angle (and ensuing roll moment) from growing too large.

H. Discussion of Results

The dominance of the divergent Dutch-roll and roll-resonance modes has critical ramifications for the stability and control properties of LAR wings. First and foremost, the presence of these modes can be uniquely attributed to the derivatives created by roll stall and the low moments of inertia, which are inherent to these wings. The subsequent creation of a significant roll stability derivative L_β due to the tip-vortex asymmetry of a LAR wing in sideslip is seen here to induce unstable oscillations of all lateral variables; the dependence of this response upon angle of attack

perturbations through roll-resonance demonstrates a fundamental coupling of the lateral and longitudinal stability axes, which is not present for conventional aircraft flying at equilibrium conditions. The tendency of LAR wings to submit to this mode after only minor perturbations from trim conditions indicates their vulnerability to instabilities when small, nonzero sideslip conditions exist.

The modes discussed in this paper are additionally interesting, as they can be described as purely aerodynamic; unlike conventional stability modes for high-aspect-ratio aircraft, they are entirely attributed to the loading asymmetries of roll stall as opposed to the size and orientation of geometric features, such as tail surfaces. A consideration of this mode has significant impact on future vehicle design of MAVs, as control surfaces must be sized to compensate for wings with their own inherently unstable dynamics. A previous work by the authors has indicated the potential for winglets centered below the center of gravity of the wing to reduce the magnitude of roll stall, and thus, the associated stability derivative L_β [21]. As weight is always a concern for MAV designers, a potential solution that would not increase the airframe weight is the implementation of a yaw damper, which would actively serve to augment the N_r derivative. The most crucial impact of this investigation, however, is the understanding of the creation and influence of the divergent Dutch-roll and roll-resonance modes experienced by LAR wings, which have not previously been accounted for in MAV design. In essence, this demonstrates the ineffectiveness of conventional design tools, which do not compensate for the unstable dynamics of the wing itself.

V. Conclusions

This paper presents new results for the stability and control properties of LAR wings. To date, the uncertainties associated with the low-Reynolds-number aerodynamic regime have made using these wings in MAV design an iterative exercise. Limited information exists about the static loads experienced by MAV wings, although recent results by the authors and others have provided some canonical aerodynamic studies of longitudinal and lateral forces and moments. The first discussions of roll stall for LAR wings came out of such papers, and this previously unconsidered inherent aerodynamic load, generated on models bereft of geometric features that roll moments are conventionally attributed to, suggested the need for a better characterization of the lateral-stability-response characteristics of the wings themselves. Experimental challenges have prevented a comprehensive study of damping stability derivatives for these wings; for this reason, an active positioning system was designed and built by the group to estimate these parameters. This knowledge is then incorporated into a full model for the flight dynamics of LAR wings, and is used to simulate the response to perturbations from equilibrium (trim) conditions.

Numerical integrations of the equations of motion indicated that, even for small disturbances, the response of the wing was dominated by unstable oscillatory behavior with coupled interactions between the state variables β , ϕ , p , and r . Favorable comparisons with a linearized approximation permitted the use of a linear stability analysis, which suggests that this response is similar to that of an unstable Dutch roll. The stability derivatives associated with the unique aerodynamic loading of LAR wings thus cause these wings to be naturally susceptible to unstable modes, which must be compensated for when developing a full MAV. Furthermore, unlike a traditional Dutch roll where lateral and longitudinal perturbations

Table 3 Effects of scaled stability derivatives on eigenvalues at $\alpha_0 = 5$ deg

Scaling factor	Scaled derivative	λ
1	L_β, N_β	$1.1 \pm 5.7i$
1/11	L_β	$-0.001 \pm 4.3i$
1/20	L_β	$-0.14 \pm 4.2i$
6	N_β	$-0.003 \pm 12.1i$
20	N_β	$-0.21 \pm 21.9i$

can be entirely decoupled, angle of attack variations were seen to interact with the lateral state variables and fundamentally alter the nature of the response. A new behavior, referred to as roll-resonance, was seen to occur when short-period longitudinal oscillations [$\alpha(t) \sim \sin(\omega_a t)$] were imposed with a frequency close to the natural frequency of the Dutch-roll response. The interactions between the angle of attack and the sideslip angle resulted in antisymmetric restoring roll moments and an ensuing bank-angle divergence, which inherently cross couples the lateral and longitudinal stability axes. This behavior of LAR wings at equilibrium flight conditions is representative of the difficulties involved with designing MAVs; however, with the improved understanding of the wing dynamics developed in this paper, better passive and active stabilization methods can be implemented to greatly simplify the challenges of future vehicle design and automation.

References

- [1] Grasmeyer, J., and Keennon, M., "Development of the Black Widow Micro Air Vehicle," *39th AIAA Aerospace Sciences Meeting and Exhibit*, AIAA Paper 2001-0127, Jan. 2001.
- [2] Hundley, R., and Gritton, E., "Future Technology-Driven Revolutions in Military Operations," RAND Corp., Document No. DB-110-ARPA, Santa Monica, CA, 1994.
- [3] Stanford, B., Abdulrahim, M., Lind, R., and Ifju, P., "Investigation of Membrane Actuation for Roll Control of a Micro Air Vehicle," *Journal of Aircraft*, Vol. 44, No. 3, 2007, pp. 741–749. doi:10.2514/1.25356
- [4] Albertani, R., Stanford, B., DeLoach, R., Hubner, J., and Ifju, P., "Wind-Tunnel Testing and Modeling of a Micro Air Vehicle with Flexible Wings," *Journal of Aircraft*, Vol. 45, No. 3, 2008, pp. 1025–1032. doi:10.2514/1.33338
- [5] de Croon, G., Groen, M., Wagter, C. D., Remes, B., Ruijsink, R., and van Oudheusden, B., "Design, Aerodynamics and Autonomy of the DelFly," *Bioinspiration & Biomimetics*, Vol. 7, No. 2, May 2012, Paper 025003. doi:10.1088/1748-3182/7/2/025003
- [6] Wood, R., "The First Takeoff of a Biologically Inspired At-Scale Robotic Insect," *IEEE Transactions on Robotics*, Vol. 24, No. 2, April 2008, pp. 341–347. doi:10.1109/TRO.2008.916997
- [7] Spedding, G., and McArthur, J., "Span Efficiencies of Wings at Low Reynolds Numbers," *Journal of Aircraft*, Vol. 47, No. 1, 2010, pp. 120–128. doi:10.2514/1.44247
- [8] Yang, S., and Spedding, G., "Spanwise Variation in Circulation and Drag of Wings at Moderate Reynolds Number," *Journal of Aircraft*, Vol. 50, No. 3, 2013, pp. 791–797. doi:10.2514/1.C031981
- [9] Taira, K., and Colonius, T., "Three-Dimensional Flows Around Low-Aspect-Ratio Flat-Plate Wings at Low Reynolds Numbers," *Journal of Fluid Mechanics*, Vol. 623, March 2009, pp. 187–207. doi:10.1017/S0022112008005314
- [10] Ellington, C., van der Berg, C., Willmott, A., and Thomas, A., "Leading-Edge Vortices in Insect Flight," *Nature*, Vol. 384, No. 6610, Dec. 1996, pp. 626–630. doi:10.1038/384626a0
- [11] Dickinson, M., and Gotz, K., "Unsteady Aerodynamic Performance of Model Wings at Low Reynolds Numbers," *Journal of Experimental Biology*, Vol. 174, Jan. 1993, pp. 45–64.
- [12] Swanton, E., Vanier, B., and Mohseni, K., "Flow Visualization and Wall Shear Stress of a Flapping Model Hummingbird Wing," *Experiments in Fluids*, Vol. 49, No. 3, 2010, pp. 657–671. doi:10.1007/s00348-010-0832-1
- [13] Jian, T., and Ke-Qin, Z., "Numerical and Experimental Study of Flow Structure of Low Aspect Ratio Wing," *Journal of Aircraft*, Vol. 41, No. 5, 2004, pp. 1196–1201. doi:10.2514/1.5467
- [14] Gresham, N., Wang, Z., and Gursul, I., "Low Reynolds Number Aerodynamics of Free-to-Roll Low Aspect Ratio Wings," *Experiments in Fluids*, Vol. 49, No. 1, 2010, pp. 11–25. doi:10.1007/s00348-009-0726-2
- [15] Arena, A., and Mueller, T., "Laminar Separation, Transition, and Turbulent Reattachment near the Leading Edge of Airfoils," *AIAA Journal*, Vol. 18, No. 7, 1980, pp. 747–753. doi:10.2514/3.50815
- [16] Selig, M., Guglielmo, J., Broeren, A., and Giguere, P., *Summary of Low Speed Airfoil Data*, Vol. 1, SoarTech, Virginia Beach, VA, 1996, pp. 23–53.
- [17] Pelletier, A., and Mueller, T., "Low Reynolds Number Aerodynamics of Low-Aspect-Ratio, Thin/Flat/Cambered-Plate Wings," *Journal of Aircraft*, Vol. 37, No. 5, 2000, pp. 825–832. doi:10.2514/2.2676
- [18] Torres, G., and Mueller, T., "Low-Aspect-Ratio Wing Aerodynamics at Low Reynolds Numbers," *AIAA Journal*, Vol. 42, No. 5, 2004, pp. 865–873. doi:10.2514/1.439
- [19] Shields, M., and Mohseni, K., "Effects of Sideslip on the Aerodynamics of Low Aspect Ratio Wings at Low Reynolds Numbers," *AIAA Journal*, Vol. 50, No. 1, 2012, pp. 85–99. doi:10.2514/1.J051151
- [20] Shields, M., and Mohseni, K., "Roll Stall for Low-Aspect-Ratio Wings," *Journal of Aircraft*, Vol. 50, No. 4, July 2013, pp. 1060–1069. doi:10.2514/1.C031933
- [21] Shields, M., and Mohseni, K., "Passive Mitigation of Roll Stall for Low Aspect Ratio Wings," *Advanced Robotics: Special Issue on Aerial Robots*, Vol. 27, No. 9, April 2013, pp. 667–681. doi:10.1080/01691864.2013.778941
- [22] Thomasson, P., "The Flight Dynamics of a Gust Insensitive Unmanned Aircraft," *IEE Colloquium on Control and Guidance of Remotely Operated Vehicles*, Vol. 6, Institution of Engineering and Technology, Hertfordshire, England, U.K., 1995, pp. 6/1–6/3. doi:10.1049/ic:19950802
- [23] Pisano, W. J., and Lawrence, D. A., "Autonomous Gust Insensitive Aircraft," *AIAA Guidance, Navigation, and Control Conference and Exhibit*, AIAA, Reston, VA, Aug. 2008; also AIAA Paper 2008-6510.
- [24] Zimmerman, C., "An Analysis of Lateral Stability in Power-Off Flight with Charts for Use in Design," NACA TR-521, 1935.
- [25] Shortall, J., "Effect of Tip Shape and Dihedral on Lateral-Stability Characteristics," NACA TR-548, 1935.
- [26] Phillips, W., "Effect of Steady Rolling on Longitudinal and Directional Stability," NACA TN-627, June 1948.
- [27] Phillips, W., *Mechanics of Flight*, 2nd ed., Wiley, Hoboken, NJ, 2010, pp. 377–411, 715–939.
- [28] Phillips, W., "Improved Closed-Form Approximation for Dutch Roll," *Journal of Aircraft*, Vol. 37, No. 3, 2000, pp. 484–490. doi:10.2514/2.2623
- [29] Shields, M., and Mohseni, K., "Aerodynamic Damping Derivatives for Low Aspect Ratio Wings at Low Reynolds Numbers," *43rd AIAA Fluid Dynamics Conference*, AIAA Paper 2013-3192, June 2013.
- [30] Nelson, R. C., and Pelletier, A., "The Unsteady Aerodynamics of Slender Wings and Aircraft Undergoing Large Amplitude Maneuvers," *Progress in Aerospace Sciences*, Vol. 39, Nos. 2–3, 2003, pp. 185–248. doi:10.1016/S0376-0421(02)00088-X
- [31] Gursul, I., Gordnier, R., and Visbal, M., "Unsteady Aerodynamics of Nonslender Delta Wings," *Progress in Aerospace Sciences*, Vol. 41, No. 7, 2005, pp. 515–557. doi:10.1016/j.paerosci.2005.09.002
- [32] Katz, J., "Wing/Vortex Interactions and Wing Rock," *Progress in Aerospace Sciences*, Vol. 35, No. 7, 1999, pp. 727–750. doi:10.1016/S0376-0421(99)00004-4
- [33] Gülçat, U., *Fundamentals of Modern Unsteady Aerodynamics*, Springer-Verlag, Berlin-Heidelberg, 2010, pp. 251–258, 264–289.
- [34] Schmidt, L. V., *Introduction to Aircraft Flight Dynamics*, AIAA, Reston, VA, 1998, pp. 9–42, 207–233, 237–248, 257–275.
- [35] Leishman, J. G., *Principles of Helicopter Aerodynamics*, 2nd ed., Cambridge Univ. Press, New York, 2006, pp. 306–315, 323–326, 333–342, 378–412.
- [36] Carroll, J. V., and Mehra, R. V., "Bifurcation Analysis of Nonlinear Aircraft Dynamics," *Journal of Guidance, Control, and Dynamics*, Vol. 5, No. 5, 1982, pp. 529–536. doi:10.2514/3.56198
- [37] Gilmore, R., *Catastrophe Theory for Scientists and Engineers*, Courier Dover, Toronto, Ontario, 1993, pp. 296–317.
- [38] Owens, D., Brandon, J., Croom, M., Fremaux, C., Heim, E., and Vicroy, D., "Overview of Dynamic Test Techniques for Flight Dynamics Research at NASA LaRC (Invited)," *25th AIAA Aerodynamic Measurement Technology and Ground Testing Conference*, AIAA Paper 2006-3146, June 2006.
- [39] Fisher, L., and Wolhard, W., "Some Effects of Amplitude and Frequency on the Aerodynamic Damping of a Model Oscillating Continuously in Yaw," NACA TN-2766, Sept. 1952.

- [40] Bird, J., Fisher, L., and Hubbard, S., "Some Effects of Frequency on the Contribution of a Vertical Tail to the Free Aerodynamic Damping of a Model Oscillating in Yaw," NACA TR-1130, April 1953.
- [41] Babcock, J., Albertani, R., and Abate, G., "Experimental Estimation of the Rotary Damping Coefficients of a Pliant Wing," *Journal of Aircraft*, Vol. 49, No. 2, 2012, pp. 390–397. doi:10.2514/1.C031161
- [42] Jones, W., "Wind-Tunnel Interference Effects on Measurements of Aerodynamic Coefficients for Oscillating Aerofoils," Aeronautical Research Council TR Rept. and Memorandum No. 2786, Sept. 1950.
- [43] Braslow, A., Wiley, H., and Lee, C., "A Rigidly Forced Oscillation System for Measuring Dynamic-Stability Parameters in Transonic and Supersonic Wind Tunnels," NACA TN-D-1231, March 1962.
- [44] Beam, B., "A Rigidly Forced Oscillation System for Measuring Dynamic-Stability Parameters in Transonic and Supersonic Wind Tunnels," NACA TR-1258, 1956.
- [45] Tomek, D., Sewall, W., Mason, S., and Szchur, B., "The Next Generation of High-Speed Dynamic Stability Wind Tunnel Testing (Invited)," *25th AIAA Aerodynamic Measurement Technology and Ground Testing Conference*, AIAA Paper 2006-3148, June 2006.
- [46] Schueler, C., Ward, L., and Hodapp, A. E., Jr., "Techniques for Measurement of Dynamic Stability Derivatives in Ground Test Facilities," AGARDograph 121, Oct. 1967.
- [47] Morris, S. J., and Holden, M., "Design of Micro Air Vehicles and Flight Test Validation," *Proceedings of the Conference on Fixed, Flapping and Rotary Wing Vehicles at Very Low Reynolds Numbers*, Univ. of Notre Dame, Notre Dame, IN, June 2000, pp. 153–176.